ACS Photonics

Article

pubs.acs.org/journal/apchd5

Subfemtosecond and Nanometer Plasmon Dynamics with Photoelectron Microscopy: Theory and Efficient Simulations

Timothy J. Davis,*[,†,‡] Bettina Frank,[‡] Daniel Podbiel,[§] Philip Kahl,[§] Frank-J. Meyer zu Heringdorf,*[,§] and Harald Giessen*[,‡]

[†]School of Physics, University of Melbourne, Parkville, Victoria 3010, Australia

[‡]4th Physics Institute and Research Center SCoPE, University of Stuttgart, 70569 Stuttgart, Germany

[§]Faculty of Physics and Center for Nanointegration, Duisburg-Essen (CENIDE), University of Duisburg-Essen, 47048 Duisburg, Germany

S *Supporting Information*

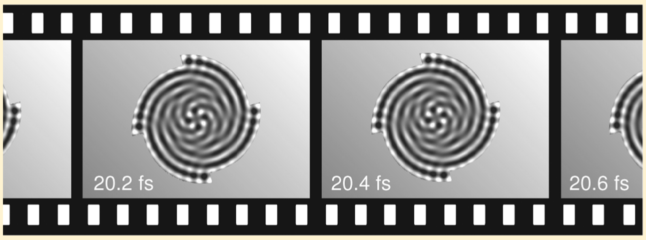

ABSTRACT: We develop a theoretical model of the excitation and interference of surface plasmon polariton (SPP) waves with femtosecond laser pulses and use the model to understand the features in images from subfemtosecond time-resolved two-photon photoelectron microscopy (2PPE−PEEM). The numerically efficient model is based on the optics of SPP modes on multilayer thin films and takes account of the excitation and interference by the incident light, its polarization, the boundary shape on the film where the plasmons are generated, the pulsed form of the excitation and the time integration associated with the PEEM method. The model explains the dominant features observed in the images including the complex patterns formed in experiments involving orbital angular momentum. The model forms the basis of an efficient numerical method for simulating time-resolved 2PPE−PEEM images of SPP wave propagation. The numerics is extremely fast, efficient, and accurate, so that each image can take as little as a few seconds to calculate on a laptop computer, enabling entire PEEM movies to be calculated within minutes.

KEYWORDS: *surface plasmon polaritons, orbital angular momentum, interference, excitation, numerical*

Surface plasmon polaritons (SPPs) are electromagnetic waves coupled to the conduction electrons of a metal that propagate along metal−dielectric interfaces.[1−4] In thin metal films, the coupling between the SPPs on the upper and lower surfaces leads to two propagating eigenmodes.[5] One of the modes has most of the electric field outside the metal, reducing Ohmic resistance and resulting in long-range propagation.[6] The other mode has more of the SPP electric field confined within the metal and is characterized by high damping losses[7−12] and therefore short propagation lengths, making these modes more difficult to study. Short-range SPPs have been investigated using metal−insulator−metal (MIM) waveguides, where the plasmon wavelength was reduced to 51 nm for 650 nm excitation wavelength.[13] There have been some attempts to explore the potential of long- and short-range surface plasmons for imaging[14] and focusing.[15−21] However, the techniques used in these experiments provide only static information about SPP waves on surfaces. For example, scanning near-field optical microscopy (SNOM) yields images of the steady-state intensity distributions or interference patterns.

Recent experiments using time-resolved two-photon photoemission (2PPE) combined with photoemission electron microscopy (PEEM)[22−28] have provided dynamic information on SPP wave propagation, including both long- and short-range modes. This method derives from studies of metal surfaces[29,30] in which a laser pulse directed onto a metal surface excites the conduction electrons, with a distribution that is probed a short time later by a second laser pulse. The energy provided by two-photon absorption is sufficient to eject electrons from the surface, which can then be used for image formation in an electron microscope. Changing the time delay between pulses leads to information about the time evolution of the excited electron distribution. Since the electron yield in the 2PPE−PEEM experiment is low, a large number of repeated laser pulses is required to build an image with acceptably low levels of shot noise. The time-integration required by this process adds another level of complexity to the interpretation of the photoelectron images.

In this paper we analyze the excitation and interaction processes between SPPs and femtosecond laser pulses and model the 2PPE−PEEM process used to create images of SPP excitation and include the effect of the time integration, which results in a model linking the properties of the SPPs and the electron microscope image. The model is based on the optics of SPP excitation and propagation on multilayer thin films, with the two-photon emission proportional to the fourth power of

Received: June 26, 2017
Published: September 7, 2017

DOI: 10.1021/acsphotonics.7b00676
ACS Photonics XXXX, XXX, XXX−XXX

the total electric field distribution on the metal surface. We compare experimental 2PPE−PEEM images with the model, in particular, recent experiments using orbital angular momentum,[28,31] which allows us to identify the physical mechanisms underpinning the key features. The model provides an efficient method for the numerical simulation of time-resolved 2PPE−PEEM images and movies of SPP waves propagating on metal films with complicated boundaries. Importantly, the theory underpinning the model leads to expressions for the vector electric field of the SPP wave excited from arbitrary-shaped boundaries. These expressions can be used to model other experiments, such as those performed with Scanning Near-field Optical Microscopy (SNOM) and provide insights into the vector properties of SPPs with orbital angular momentum.

■ TIME-RESOLVED 2PPE−PEEM OF SURFACE PLASMONS

Excitation of Surface Plasmons. To model the photoelectron yield from the metal surface, we assume the total electric field at any point can initiate a two-photon absorption process resulting in electron emission. Coherent two-photon absorption is associated with the third-order nonlinearity of the electric susceptibility of the material.[32] For isotropic materials where the polarization and field directions are parallel, the polarizability induced by the third-order nonlinearity can be expressed in terms of an effective susceptibility $\mathbf{P}^{(3)} = \epsilon_0\chi^{(3)}|\mathbf{E}|^2\mathbf{E}$, where it is assumed that the nonlinear mixing occurs at the one frequency $\pm\omega$. The absorption is then proportional to $\mathrm{Im}(\mathbf{P}^*\cdot\mathbf{E}) = \epsilon_0\chi^{(3)*}|\mathbf{E}|^4$. In our derivation we take the laser light incident normal to the surface, a configuration that has been used recently for 2PPE−PEEM experiments.[31,33] The laser pulses incident on edges, grooves, or ridges in the metal surface induce oscillating surface charges that launch the surface plasmon waves. Since the electrons are ejected from the surface of the metal, for simplicity we only model the surface plasmon electric field at the top of the metal and take the electron yield proportional to the fourth power of the total electric field (Figure 1).

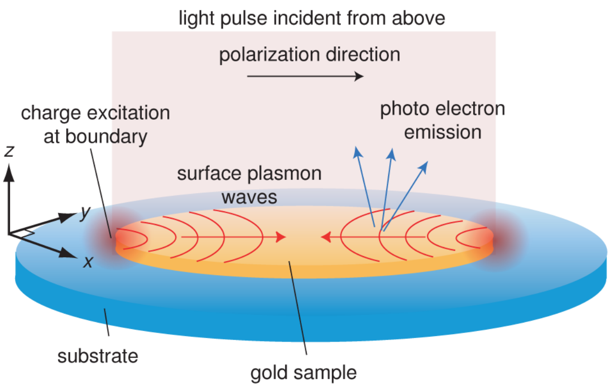

Figure 1. Sketch of the 2PPE−PEEM process that generates surface plasmons at the boundary of a gold film on a substrate.

The 2PPE−PEEM experiment requires a conducting substrate, which in our experiments consists of silicon with the gold film or crystal on top. Since silicon has a thin native oxide layer, the sample is a multilayer thin-film on a silicon substrate. The properties of surface plasmon polaritons (SPPs) associated with a multilayer thin film structure can be derived from Maxwell's equations by seeking solutions for self-sustained (although damped) oscillations.[5] With the films lying in the $x - y$ plane, where $\mathbf{r} = x\hat{x} + y\hat{y}$ and with the permittivity $\epsilon(z)$ piecewise continuous in z, the wave equation for the plasmon vector potential $\mathbf{A}_p(\mathbf{r}, z) = \mathbf{A}_r(\mathbf{r})u(z)$ can be separated into two equations

$$\nabla_r^2\mathbf{A}_r(\mathbf{r}) + \alpha^2\mathbf{A}_r(\mathbf{r}) = \kappa\hat{r}(\hat{n}\cdot\hat{e})\delta(\mathbf{r} - \mathbf{r}_b)E_I \tag{1}$$

and

$$\frac{\partial^2 u(z)}{\partial z^2} + (k^2\epsilon(z) - \alpha^2)u(z) = 0 \tag{2}$$

where $k = \omega/c$ is the wavenumber and ∇_r^2 is the two-dimensional Laplacian in the $x - y$ plane. The equation for the in-plane vector potential $\mathbf{A}_r(\mathbf{r})$ contains a source term that is nonzero at boundaries located at $\mathbf{r}_b$ in the metal film, where the incident light field $\mathbf{E}_I = E_I\hat{e}$ induces a surface charge $\sigma = (\epsilon_b - \epsilon_m)\hat{n}\cdot\mathbf{E}_I$ to drive the plasmon oscillations, with $\epsilon_b - \epsilon_m$ the permittivity difference across the boundary. The source of the plasmon vector potential $\kappa\hat{r}(\hat{n}\cdot\hat{e})\delta(\mathbf{r} - \mathbf{r}_b)E_I$ in the direction $\hat{r}$ is proportional to this surface charge, where κ is a constant and $\hat{n}$ is a unit vector normal to the boundary. The solution of eq 2 yields a set of eigenvalues α that are the propagation constants for the different plasmon modes in the multilayer film,[5] with $u(z) = \exp(-\gamma z)$, $\gamma^2 = \alpha^2 - \epsilon_m k^2$ and ϵ_m is the relative permittivity of the metal at the top surface $z = 0$. (Note the definition of γ here differs from that of Davis[5] − this parameter has a large imaginary component, but here we redefine it to make the imaginary part explicit so that γ is predominantly real.)

To solve the inhomogeneous problem eq 1 we find the Green's function in the $x - y$ plane,[34] which yields a solution

$$\mathbf{A}_r(\mathbf{r}) \approx (E_L/k^2)\int(\gamma\hat{r}_s + i\alpha\hat{z})(\hat{e}\cdot\hat{n}')H_0^{(1)}(\alpha r_s)\mathrm{d}^2r' \tag{3}$$

where $H_0^{(1)}(\alpha r) = J_0(\alpha r) + iY_0(\alpha r)$ is the Hankel function of the first kind involving Bessel functions $J_0(\alpha r)$ and $Y_0(\alpha r)$. The Hankel function is the exact solution to the problem of the initiation and propagation of a wave from an arbitrarily shaped boundary in two dimensions. The normal to the ridge or boundary edge where the surface charge is excited is $\hat{n}' = \hat{n}(\mathbf{r}')\delta(\mathbf{r}' - \mathbf{r}_b)$, which depends on position, and the delta function sets $\hat{n}' \neq 0$ only when $\mathbf{r}'$ locates a point on a line (such as a groove or ridge) where the incident light can excite a plasmon. For brevity, we set $\mathbf{r}_s = \mathbf{r} - \mathbf{r}'$ and $r_s = |\mathbf{r}_s|$ as the distance from the source point $\mathbf{r}'$ to the point of observation and $\hat{r}_s = \mathbf{r}_s/r_s$. The $\hat{z}$ component was found by requiring that $\nabla\cdot\mathbf{A}_p = 0$ away from the source. This requires a derivative $\mathrm{d}H_0^{(1)}(x)/\mathrm{d}x \approx iH_0^{(1)}(x)$, where the approximation is very good when $x = \alpha r_s > 3$ or $r_s > \lambda_p/2$ is greater than about half a plasmon wavelength λ_p from the source. The factor E_L absorbs the unknown constants such as the amplitude of the incident field and the efficiency of excitation of the plasmons. The electric field $\mathbf{E}_p = ik\mathbf{A}_p$ is then

$$\mathbf{E}_p(\mathbf{r}, z) \approx E_L e^{-\gamma z}\int\frac{(i\gamma\hat{r}_s - \alpha\hat{z})}{k}(\hat{e}\cdot\hat{n}')H_0^{(1)}(\alpha r_s)\mathrm{d}^2r' \tag{4}$$

Since we are interested in the electric field at the surface of the metal, we set $z = 0$ and no longer show the z dependence explicitly.

In the ideal case of an infinitely long boundary line, the solution of eq 4 reduces to a plane wave propagating in a direction $\hat{n}$ normal to the line, given by

DOI: 10.1021/acsphotonics.7b00676
ACS Photonics XXXX, XXX, XXX−XXX

$$\mathbf{E}_p(\mathbf{r}) \approx E_L(\hat{e}\cdot\hat{n})\left(\frac{i\gamma\hat{n} - \alpha\hat{z}}{k}\right)e^{i\alpha r} \tag{5}$$

where r is the perpendicular distance from the line. Since the boundary normal contains the delta function, the surface integral over the boundary reduces to a line integral along the boundary. The plane wave solution eq 5 is for a single frequency,[5] since γ and α depend on $k = \omega/c$. For a distribution of frequencies, $g(\omega')$, as occurs with an incident pulse of light, the time variation of the wave is obtained from the Fourier transform of $\mathbf{E}_p(\mathbf{r},\omega')\, g(\omega')\, \exp(-i\omega' t)$ with respect to ω'. We model the incident light pulse by a Gaussian function centered at frequency ω. When multiplied into eq 5 and Fourier transformed, we obtain

$$\mathbf{E}_p(\mathbf{r}, t) = E_L(\hat{e}\cdot\hat{n})\left(\frac{i\gamma\hat{n} - \alpha\hat{z}}{k}\right)G_a(r, t)e^{i\alpha r - i\omega(t - t_a)} \tag{6}$$

The Gaussian $g(\omega')$ is transformed into a pulse of width Δt in the time domain that we take centered at time t_a,

$$G_a(r, t) = \exp\left(-\frac{4(\alpha' r - \omega(t - t_a))^2}{\omega^2 \Delta t^2}\right) \tag{7}$$

where $\alpha = \alpha' + i\alpha''$ is resolved into real and imaginary components. In the derivation we assumed that α varies linearly with frequency about the center frequency ω of the pulse. We then evaluate α at ω, which is equivalent to neglecting dispersion of the wavepacket. As defined, eq 7 produces a Gaussian profile with a full-width of Δt between the e^{-1} points.

To include the time response of the SPP for an arbitrary boundary we could use eq 4 and take the Fourier transform over frequency. However, the result is difficult to obtain in closed form and numerical evaluation is computationally intensive. Instead we use the plane-wave solution as a guide and consider an approximate solution based on eq 4 but replace the plane wave in eq 6 by the Hankel function

$$\begin{aligned}\mathbf{E}_p(\mathbf{r}, t) &\approx E_L G_a(r, t)e^{-i\omega(t - t_a)}\int\left(\frac{i\gamma\hat{r}_s - \alpha\hat{z}}{k}\right)(\hat{e}\cdot\hat{n}')H_0^{(1)}(\alpha' r_s)e^{-\alpha'' r_s}\mathrm{d}^2 r' \\ &= \mathbf{E}_p(\mathbf{r})G_a(r, t)e^{-i\omega(t - t_a)}\end{aligned} \tag{8}$$

which leads to an expression for the SPP generated from an arbitrary boundary by a pulse of light. This equation has the correct asymptotic forms for an infinitely long boundary, which reproduces eq 6, and for the infinitely long pulse, which is eq 4.

To simulate the 2PPE experiment on a metal film with a complicated shape, the boundary is represented by a set of straight line segments. Provided enough line segments are used such that any deviations from the true boundary are much smaller than the plasmon wavelength, we would expect the model to accurately represent the plasmon wave away from the boundary. In practice, the integral is evaluated numerically over each line segment on the boundary. For an infinite line, this equation reproduces the plane wave result. The Hankel function in eq 8 represents a Huygens' wavelet propagating in two dimensions and the emission from the boundary is obtained by a sum of these wavelets, as given by the integral. An example is shown in Figure 2.

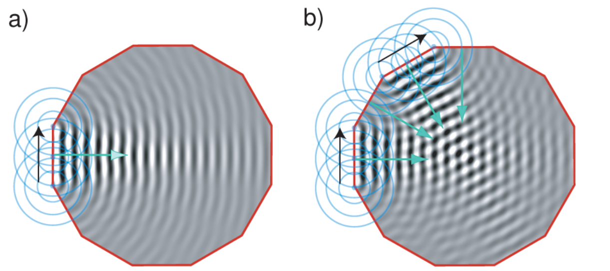

Figure 2. Example showing how plasmons are simulated by representing a complicated boundary by straight line segments. (a) Each line segment on the boundary is divided into sources of Huygens' wavelets, calculated from the Hankel function $H_0^{(1)}(\alpha' r)$. The response of an individual line is the sum of all the source points (represented by the arrow), which is equivalent to the integral eq 8. (b) Sum of the wave contributions from all the source lines leads to interference patterns; two line contributions are shown in the figure.

Photoemission Process. In the photoelectron microscopy experiment, electrons are ejected from the metal by two optical pulses and the resulting electron emission is integrated over a long period of time. The first pulse interacts with the entire surface of the metal and launches a plasmon wave $\mathbf{E}_{p,1}$ from the boundary $\mathbf{r} = \mathbf{r}_0$ at time t_1. The second pulse centered at time t_2 generates a surface plasmon wave $\mathbf{E}_{p,2}$ that also propagates from $\mathbf{r} = \mathbf{r}_0$. For multiple boundaries, or lines of plasmon sources, we can generalize the surface plasmon source position to $\mathbf{r}_n$ for the nth source line with plasmon propagation direction $\hat{n}_n$. It is also useful to separate the Gaussian pulse from the position dependence of the wave, as in eq 8, so that the plasmon propagating from the nth boundary is $\mathbf{E}_{p,a}(\mathbf{s}_n, t) = \mathbf{E}_{p,a}(\mathbf{s}_n)\, G_a(s_n, t)\exp(-i\omega(t - t_a))$, where $\mathbf{s}_n = \mathbf{r} - \mathbf{r}_n$. The total electric field at some time t at the metal surface is given by the sum of the two incident light pulses, $\mathbf{E}_{I,1}$ and $\mathbf{E}_{I,2}$, and the sum of all the surface plasmons they produce. To simplify the expressions, we number the plasmon sources from $n = 1$ to N and let $n = 0$ represent the incident light pulses, so that the total electric field can be written as

$$\mathbf{E}_T = \sum_{n=0}^{N}\sum_{a=1}^{2}\mathbf{E}_{n,a}(\mathbf{s}_n)G_a(s_{n,t})e^{-i\omega(t - t_a)} \tag{9}$$

where a is summed from 1 to 2, representing the two pulses.

The coherent two-photon absorption that leads to electron emission is proportional to $I^2 = (\mathbf{E}_T^*\cdot\mathbf{E}_T)^2$ and the PEEM signal measured in an experiment is proportional to the square of the intensity integrated over all time. From eq 9, we can write the PEEM signal as

$$P_c = \int_{-\infty}^{\infty}\left|\sum_{n=0}^{N}\sum_{a=1}^{2}\mathbf{E}_{n,a}(\mathbf{s}_n)G_a(s_n, t)e^{i\omega t_a}\right|^4 \mathrm{d}t \tag{10}$$

Note that by taking the modulus-square, the common time factor $\exp(-i\omega t)$ no longer appears, leaving only the Gaussian envelope $G_a(s_n, t)$ depending on time. As shown in eq 10, the incident light and plasmon electric fields have fixed profiles with position over the surface (given by $\mathbf{E}_{n,a}(\mathbf{s}_n)$) but are modulated by a traveling Gaussian pulse $G_a(s_n, t)$ that depends only on s_n, the distance from the line in the direction of the normal. This means the complex field vectors including $e^{i\omega t_a}$ can be precomputed at each position on the surface and those corresponding to a given time delay t_a summed together. For the time integral, these sums are multiplied by the appropriate Gaussian envelope $G_a(s_n, t)$ evaluated at each time step and summed together, thus, performing the integration. Moreover, the time step dt required in the integral needs only to be small enough to integrate the Gaussian envelope, which varies over a time Δt, being the width of the light pulse, rather than over a time $1/\omega$ being the period of the light wave that is much

DOI: 10.1021/acsphotonics.7b00676
ACS Photonics XXXX, XXX, XXX−XXX

smaller. Thus, we find that only a small number of terms are required to perform the integral, which then becomes efficient to compute. This procedure, although approximate, greatly speeds up the computation and enables us to generate many simulations as functions of pulse delay time.

Recently it was shown that the efficiency of the 2PPE emission depends on the vector direction of the electric field relative to the surface normal,[35] with the emission from the in-plane fields weaker than the emission from the out-of-plane fields. It is straightforward to include this experimental finding into the model as an extra scale factor multiplying E_z. Moreover, we have complete control of the polarization states of the incident light pulses, so that more complex polarization sequences can be modeled, such as pumping with a given helicity and probing with the opposite helicity or with linearly polarized light.

General Features of 2PPE−PEEM Images. To understand the features observed in the 2PPE−PEEM experiments, it is instructive to consider one ridge or edge generating a surface plasmon with an amplitude small compared to the incident light. We assume that the two light pulses have the same polarization vector $\hat{e}$ and the amplitudes are real, so that $\mathbf{E}_1 = \hat{e}E_1$ and $\mathbf{E}_2 = \hat{e}E_2$. There are two plasmon waves generated at the boundary, one from each light pulse, propagating in direction $\hat{n}$. These waves can be written as

$$\begin{aligned}\mathbf{E}_{p,1} &= \eta(\hat{e}\cdot\hat{n})(i\gamma\hat{n} - \alpha\hat{z})E_1 e^{i\alpha s}\\ \mathbf{E}_{p,2} &= \eta(\hat{e}\cdot\hat{n})(i\gamma\hat{n} - \alpha\hat{z})E_2 e^{i\alpha s}\end{aligned} \tag{11}$$

where η is a scale factor. We first write the incident light fields as $\mathbf{E}_I(t, t_1, t_2) = \hat{e}E_I(t, t_1, t_2)$, where $E_I(t, t_1, t_2) = E_1G_1(0,t)e^{i\omega t_1} + E_2G_2(0,t)e^{i\omega t_2}$ and the plasmon fields as $\mathbf{E}_p(t, t_1, t_2, s) = \mathbf{E}_{p,1}(s) G_1(s, t)e^{i\omega t_1} + \mathbf{E}_{p,2}(s)G_2(s, t)e^{i\omega t_2}$. In the following, we suppress the time and position dependences, for the sake of brevity. The electron emission is proportional to

$$\begin{aligned}I^2 &= |\mathbf{E}_I + \mathbf{E}_p|^4\\ &= (|\mathbf{E}_I|^2 + |\mathbf{E}_p|^2 + 2\mathrm{Re}(\mathbf{E}_I^*\cdot\mathbf{E}_p))^2\\ &\approx |\mathbf{E}_I|^2\{|\mathbf{E}_I|^2 + 4\mathrm{Re}(\mathbf{E}_I^*\cdot\mathbf{E}_p)\}\end{aligned} \tag{12}$$

where quadratic and higher orders of $|\mathbf{E}_p|$ are ignored, since by assumption they are small. When integrated over time, we find a static background signal arising from $|\mathbf{E}_I|^2$, and an interference term $4\mathrm{Re}(\mathbf{E}_I^*\cdot\mathbf{E}_p)$ that depends on products of Gaussians in the form $G_1(s_1, t)G_2(s_2, t)$. If the pulse delay is long enough that the two light pulses do not overlap, then products of terms like $G_1(0,t)G_2(0,t)$ integrate to zero. Likewise, $G_1(0,t)G_2(s, t)$ is zero because the second plasmon is created after the first pulse has gone. However, we need to retain $G_2(0,t)G_1(s,t)$ because the first plasmon still exists when the second pulse arrives. This means that $|\mathbf{E}_I|^4 \approx (E_1G_1(0,t))^4 + (E_2G_2(0,t))^4$ and eq 12 can be approximated by

$$\begin{aligned}I^2 \approx{}& [E_1G_1(0, t)]^4 + [E_2G_2(0, t)]^4\\ &- 4\gamma\eta|\hat{e}\cdot\hat{n}|^2 e^{-\alpha'' s}\sin\alpha' s[E_1^4G_1^3(0, t)G_1(s, t) + E_2^4G_2^3(0, t)G_2(s, t)]\\ &- 4\gamma\eta|\hat{e}\cdot\hat{n}|^2 e^{-\alpha'' s}\sin(\alpha' s - \omega t_{21})E_1E_2^3G_1(s, t)G_2^3(0, t)\end{aligned} \tag{13}$$

The time integral of eq 13 gives

$$\begin{aligned}P_c \approx{}& \frac{\sqrt{\pi}\,\Delta t}{4}(E_1^4 + E_2^4)\\ &- \sqrt{\pi}\,\Delta t\gamma\eta|\hat{e}\cdot\hat{n}|^2 e^{-\alpha'' s}(E_1^4 + E_2^4)\sin\alpha' s e^{-3\alpha'^2 s^2/\omega^2\Delta t^2}\\ &- \sqrt{\pi}\,\Delta t\gamma\eta|\hat{e}\cdot\hat{n}|^2 e^{-\alpha'' s}E_1E_2^3\sin(\alpha' s - \omega t_{21})e^{-3(\alpha' s-\omega t_{21})^2/\omega^2\Delta t^2}\end{aligned} \tag{14}$$

This result shows three main features of the 2PPE−PEEM images of SPPs. The first term in eq 14 is the electron emission associated with the two optical pulses, with electrons emitted uniformly over the entire metal surface. These fields provide a uniform background signal. The next term is the interference between a given light pulse and the plasmon it excites. This creates a sinusoidal pattern fixed in space with a period related to the plasmon wavelength, $\lambda_p = 2\pi/\alpha'$. The fixed pattern decays with distance from the boundary, depending on the pulse width of the incident light and the decay length $1/\alpha''$ of the plasmon. The last term represents the interference between the second light pulse and the first plasmon. This also has a sinusoidal variation with a period equal to the plasmon wavelength. However, this pattern appears like a traveling wave with an amplitude peaked at a position $\alpha' s - \omega t_{21} = 0$ that depends on the light pulse delay time. A series of images of electron emission for a range of delay times t_{21} will yield information about the propagation of the plasmon waves. Such oscillatory behavior is consistent with observations of 2PPE−PEEM experiments on metal films.[31,36]

The electron yield described by eq 14 also depends on $|\hat{e}\cdot\hat{n}|^2$. Light linearly polarized at angle ψ incident on a boundary with orientation $\hat{n} = \hat{x}\cos\theta + \hat{y}\sin\theta$ launches a plasmon with an amplitude proportional to $|\hat{e}\cdot\hat{n}|^2 = \cos^2(\theta - \psi)$. For boundary orientations such that $\theta - \psi = \pm\pi/2$ there are no plasmons excited. Thus, we expect for linear polarization that the plasmon image depends on the polarization angle, which is consistent with experimental observations presented below.

With circularly polarized light the polarization vector is $\hat{e} = (\hat{x} \pm i\hat{y})/\sqrt{2}$ so that $|\hat{e}\cdot\hat{n}|^2 = 1/2$. Thus, we observe that plasmon generation and interference with the incident light is independent of the helicity ($\pm$) of the circular polarization. Moreover, since we can add multiple boundaries to eq 14 and not change the result regarding the interference between the incident light and the surface plasmons, then the helicity of the circular polarization is not observable irrespective of the boundary shape.[28] Circular polarization effects may be observable with interference between two surface plasmons propagating in different directions. For example, plasmons propagating in directions θ_1 and θ_2 will lead to an interference pattern with a cross-term $(\hat{e}^*\cdot\hat{n}_1)(\hat{e}\cdot\hat{n}_2) = \cos(\theta_2 - \theta_1) \pm i\sin(\theta_2 - \theta_1)$ that depends on the relative phase of the plasmons and the helicity of the light. To observe such interference requires relatively strong plasmon signals that can be distinguished from the incident light-plasmon interference pattern. We will show experimental evidence of this effect in the following section.

Examples of the PEEM signals calculated from eq 14 are shown in Figure 3. The input data for the calculation are obtained from the short-range plasmon listed in Table 2. The curves have been offset for clarity. The PEEM profiles show the characteristic static oscillation pattern at the boundary of the metal ($s = 0$) and a traveling wave pulse that moves with the time delay and decays with distance.

DOI: 10.1021/acsphotonics.7b00676
ACS Photonics XXXX, XXX, XXX−XXX

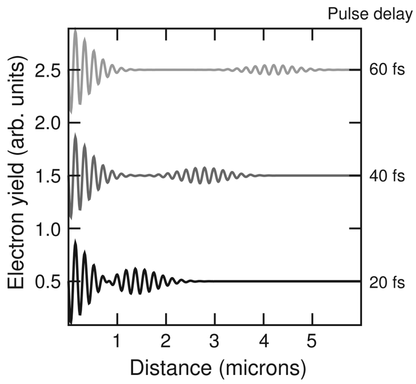

Figure 3. A PEEM signal simulated using eq 14 with data in Table 2 for the short range plasmon, showing the fixed pattern signal and a pulse that changes position with time delay (curves offset for clarity).

EXPERIMENTS AND SIMULATIONS

We have performed a large number of 2PPE−PEEM experiments on single crystals of gold machined using focused ion beams.[31] In this section we compare some of the experimental results with simulations based on the theoretical model.

SPP Focusing. In the first experiment, a 22 nm thick gold flake on a silicon substrate was milled into a circle of diameter 2 μm and a grating structure formed around it to couple the incident light into surface plasmons, which then propagate to the center of the circle. The silicon substrate has a 2.5 nm native oxide film of silica. The experiment consists of repeatedly sending two light pulses with wavelengths λ_L = 800 nm and pulse widths of about 16 fs onto the sample and integrating the electron emission over time. By collecting images of the electron emission with different delay times between each pair of pulses, the time response of the surface plasmons can be observed. However, as we have discussed previously, the integration over time creates an image that consists of the correlations and interferences between several sets of plasmons and the optical pulses.

Using the method of Davis[5] we find there are two plasmon modes associated with the gold flake. The short wavelength plasmon mode created with λ_L = 800 nm light has a wavenumber $\alpha_s = 3.58 \times 10^{-2} + i5.12 \times 10^{-4}$ nm^{-1} that corresponds to a plasmon wavelength of λ_s = 175 nm and a decay distance $1/\alpha_s''$ = 1.95 μm. The gamma factor for gold is $\gamma_s = 5.21 \times 10^{-2} - i1.00 \times 10^{-4}$ nm^{-1} that we approximate as real. The frequency of the incident light pulse is $\omega = 2.35 \times 10^{15}$ rad s^{-1}. The long wavelength plasmon mode has $\alpha_l = 8.00 \times 10^{-3} + i1.31 \times 10^{-4}$ nm^{-1} and $\gamma_l = 3.89 \times 10^{-2} - i5.75 \times 10^{-4}$ nm^{-1}.

Two images taken with different pulse delays from a series of 2PPE−PEEM experiments are shown in Figure 4 and we compare this with simulations, based on eqs 8 and 10. The parameters used in the simulation are given in Table 1. The incident light has unit amplitude $E_1 = E_2 = 1.0$ and the unknown plasmon amplitudes are adjusted to obtain a good fit to the data. The circular boundary was represented by a polygon with 32 sides. Profiles through the two sets of images are shown in Figure 5. The simulation data were scaled in amplitude and offset to align the curves with the experimental data. The simulation provides an excellent representation of the electron yield obtained in the experiments, including the excitation dependence of the orientation of the boundary relative to the direction of polarization of the incident light (simulation movies are available as Supporting Information).

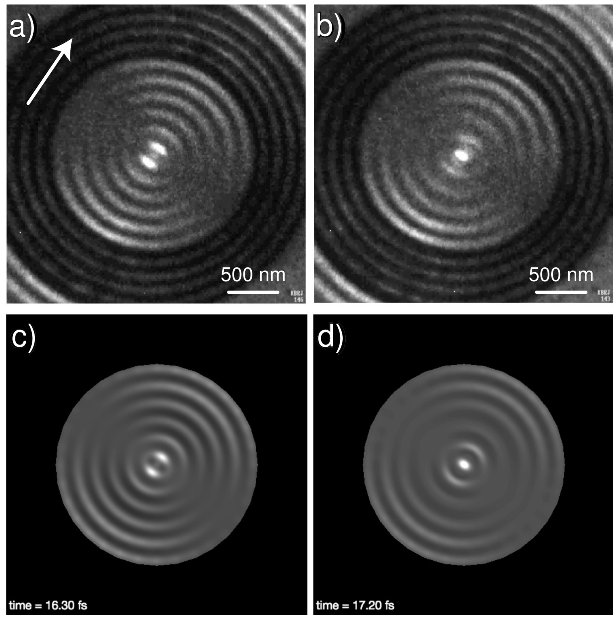

Figure 4. Comparison between experiment and the simulation for a short-range plasmon focusing experiment: (a, b) 2PPE−PEEM measurement corresponding to two time intervals between the two optical pulses. The arrow shows the direction of linear polarization of the incident beam; (c, d) simulations based on eq 10 and numerically integrating over time. The images were calculated at time delays (c) $t_2 - t_1$ = 16.3 fs and (d) $t_2 - t_1$ = 17.2 fs. The circular gold disc was modeled by a 32-sided polygon.

Table 1. Simulation Parameters for Figures 4 and 5

incident wavelength (nm)	800
incident pulse width (fs)	16
polarization angle	55°
gold thickness (nm)	22
α_s (nm^{-1})	$3.58 \times 10^{-2} + i5.12 \times 10^{-4}$
γ_s (nm^{-1})	5.21×10^{-2}
α_l (nm^{-1})	$8.00 \times 10^{-3} + i1.31 \times 10^{-4}$
γ_l (nm^{-1})	3.89×10^{-2}
amplitude ratio $(\eta_l\gamma_l)/(\eta_s\gamma_s)$	0.5

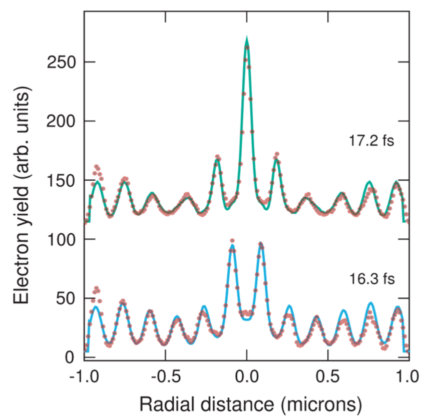

Figure 5. Experiment (points) and simulations (solid lines) for the two time delays shown in Figure 4. The simulations were scaled in amplitude to match the experimental data. The curves have been offset for clarity.

DOI: 10.1021/acsphotonics.7b00676
ACS Photonics XXXX, XXX, XXX−XXX

SPP Propagation on a Gold Flake. As another example, simulations were compared with a 2PPE−PEEM experiment on a complex gold flake, shown in Figure 6. Since the model simulates the PEEM signal from any number of straight line segments, we approximate the flake geometry with 17 straight lines. The data used in the simulation are given in Table 2 and, again, the time integral eq 10 of I^2 was performed numerically. Because of the thickness of the gold flake, the long-range surface plasmon mode has a dominant effect on the electron emission, although there is still evidence of the short-range mode. Again we see excellent agreement between the simulation and the experiment.

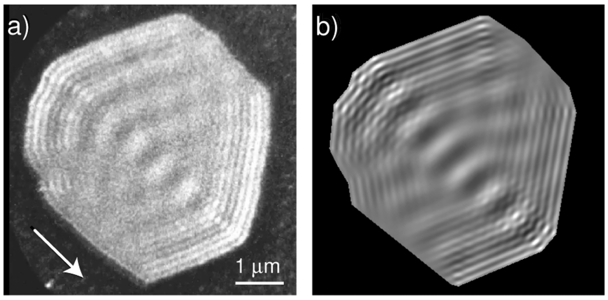

Figure 6. Experiment (a) and simulation (b) of the 2PPE−PEEM image of a gold flake calculated at $t_2 - t_1 = 12.8$ fs after coincidence of the light pulses. The arrow shows the direction of the incident linear polarization.

Table 2. Simulation Parameters for Figure 6

incident wavelength (nm)	800
incident pulse width (fs)	16
polarization angle	−45°
gold thickness (nm)	37
α_s (nm^{-1})	$3.32 \times 10^{-2} + i3.57 \times 10^{-4}$
γ_s (nm^{-1})	5.04×10^{-2}
α_l (nm^{-1})	$8.03 \times 10^{-3} + i4.62 \times 10^{-5}$
γ_l (nm^{-1})	3.87×10^{-2}
amplitude ratio $(\eta_l\gamma_l)/\eta_s\gamma_s)$	2.0

SPP Orbital Angular Momentum. Recently it was shown that boundaries cut into gold films in the form of Archimedean spirals can generate plasmons with orbital angular momentum when excited with circularly polarized light.[18,28,31] In this section we examine the theory of such structures and model the experiments on them using our efficient numerical method.

Theory of SPP Orbital Angular Momentum Excitation and Interference. To understand the features of the experiments, we take an approximate solution of the wave $\mathbf{E}_p(\mathbf{r},0)$ using eq 4. For distances far from the source (i.e., far from the boundary), the Hankel function is approximately $H_0^{(1)}(x) \approx \sqrt{2/\pi x}\ \exp(Ix - i\pi/4)$. We assume the boundary has a spiral radius that varies with angle θ according to $R_0 + l\theta/\alpha'$, where l is the integer number of wavelengths that the radius increases over an angle of 2π and R_0 is the starting radius (an example is shown in Figure 7 for $l = 1$). The observation point from the center of the spiral is $\mathbf{r} = r(\cos\phi\hat{x} + \sin\phi\hat{y})$ and the boundary is located at $\mathbf{r}' = (R_0 + l\theta/\alpha')(\cos\theta\hat{x} + \sin\theta\hat{y})$. For $r \ll R_0$ we approximate $\alpha'|\mathbf{r} - \mathbf{r}'| \approx \alpha'\ (R_0 - r\cos(\theta - \phi)) + l\theta$. Furthermore, the normal to the boundary is then approximately $\hat{n}' \approx \cos\theta\hat{x} + \sin\theta\hat{y}$. The polarization vector for circularly polarized incident light is $\hat{e}_\pm = (\hat{x} \pm i\hat{y})/\sqrt{2}$, where the $s = \pm 1$ determines the helicity, so that $\hat{e}_\pm\cdot\hat{n}' \approx e^{\pm i\theta}/\sqrt{2} = e^{is\theta}/\sqrt{2}$. The inward directed unit vector is $\hat{r}_s \approx -\hat{n}'$, which can also be expressed in polar coordinates by defining unit vectors $\hat{e}^\pm = (\hat{x} \pm i\hat{y})/\sqrt{2}$ that have the same form as the circular polarization vectors. Then we can write $\hat{r}_s = -(\hat{e}^- e^{i\theta} + \hat{e}^+ e^{-i\theta})/\sqrt{2}$. Since we are interested in the SPP fields near the center of the spiral, we can ignore losses over this small region so that the position dependence of the electric field from eq 8 is approximately

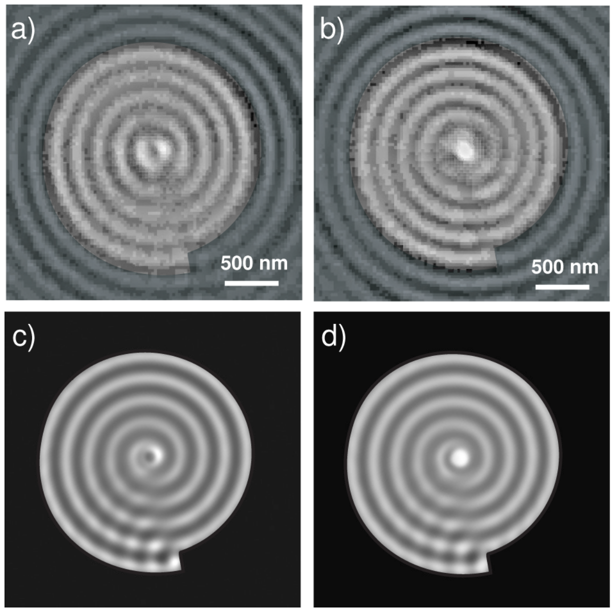

Figure 7. 2PPE−PEEM experiment (a, b) and simulation (c, d) for a spiral with a 2π phase shift anticlockwise around the boundary. (a) Left circular polarization (electric field rotating anticlockwise in the plane); (b) right circular polarization; (c) simulation LCP; (d) simulation RCP. The experimental images have been masked to highlight the plasmon spiral region; outside this region is the coupling grating and an outward propagating plasmon.

$$
\begin{aligned}
\mathbf{E}_p(r,\phi) &\approx -A\int_0^{2\pi}[(i\gamma/\sqrt{2})(\hat{e}^{(-)}e^{i\theta} + \hat{e}^{(+)}e^{-i\theta}) + \alpha\hat{z}] \\
&\times e^{is\theta}e^{il\theta - i\alpha' r\cos(\theta-\phi)}d\theta \\
&= -A\alpha\hat{z}(-i)^{l+s}e^{i(l+s)\phi}J_{l+s}(\alpha' r) \\
&- \frac{(-i)^{l+s}A\gamma}{\sqrt{2}}[\hat{e}^{(-)}e^{i(l+s+1)\phi}J_{l+s+1}(\alpha' r) - \hat{e}^{(+)}e^{i(l+s-1)\phi}J_{l+s-1}(\alpha' r)]
\end{aligned} \tag{15}
$$

with $J_n(x)$ Bessel functions of the first kind and A is a constant. The resulting plasmon field shows a complicated dependence on the orbital angular momentum l imparted by the boundary, on the helicity ($s = \pm 1$) of the excitation circular polarization, sometimes referred to as "light spin", and on the radial dependence of the electric field vector that gives rise to terms involving $\hat{e}^{(\pm)}$. Such "spin-orbit" coupling in light fields is related to the topological nature of the fields.[37,38] When this SPP field interferes with the electric field of the incident light pulse, the interference term $\mathbf{E}_I^*\cdot\mathbf{E}_p$ in eq 12 involves the complex conjugate $\hat{e}_\pm{}^*\cdot\hat{e}^{(\pm)}$. This term is zero if the two vectors have opposite helicity (i.e., − + or + −) and is nonzero otherwise. Thus, if the plasmon is probed with light of the same helicity as it is excited, the interference term involving eq 15 $\mathbf{E}_I^*\cdot\mathbf{E}_p \propto e^{il\phi}J_l(\alpha' r)$ is independent of the helicity of the circular polarization. This surprising result was predicted in the previous section and has been confirmed in recent experi-

DOI: 10.1021/acsphotonics.7b00676
ACS Photonics XXXX, XXX, XXX−XXX

ments.[18,28] If the plasmon fields are strong, which they can be near the center of the spiral, it is possible to observe interference associated with the $\hat{z}$ fields which has the form $J^2_{l\pm1}(\alpha' r)$ that does show a dependence on the helicity of the circular polarization relative to the direction of the induced orbital angular momentum. Note that by probing the SPP field with light of helicity different from the excitation field, different components of the SPP field will appear in the interference pattern. For example, exciting with $\hat{e}_+$ and probing with $\hat{e}_-$ extracts the term with $l + 1 + 1 = l + 2$, whereas probing with linearly polarized light will extract those vector field components aligned with the polarization direction.

Experiments on SPPs with Orbital Angular Momentum. In the first experiment, we examine the effect of a spiral excitation that has a single 2π phase shift around the boundary, as shown in Figure 7 for left and right circularly polarized light. The sample was a 22 μm thick gold flake, and therefore has similar plasmon modes as in Table 1. The simulation shows good agreement with the experiments assuming there is no long-range SPP mode excited. The plasmon is predominantly a short wavelength mode and there is evidence of plasmon−plasmon interference at the center. With $l = 1$ then for the two polarizations we expect the PEEM signal near the center of the spiral for plasmon−plasmon interference to follow $J^2_2(\alpha' r)$ for left circularly polarized (LCP) light and $J^2_0(\alpha' r)$ for right circularly polarized (RCP) light. The Bessel function $J_2(x)$ is zero at $x = 0$ and has its first maximum at $x = 3.06$. This means the distance to the first maximum is $r = 3.06\alpha' \approx 85$ nm, which compares reasonably with the experimental result of $r = 96 \pm 5$ nm. For RCP, $J^2_0(\alpha' r)$ is maximum at the center, which is what we observe. These findings provide good evidence that we have excited the $l = 0$ and $l = 2$ modes of the surface plasmons. Because of the simplicity of the boundary, simulation movies (available as Supporting Information) can be computed efficiently using our method, taking less than 5 min each.

It is straightforward to increase the total phase shift around the spiral by increasing the distance as a function of angle. Since all phases that differ by 2π are equivalent, the spiral can be broken into segments. An example is shown in Figure 8 that has a $4 \times 2\pi = 8\pi$ phase shift anticlockwise around the boundary or $l = 4$. This structure was milled into a gold flake 22 μm thick as in the previous example. As before, we see some difference related to the handedness of the circularly polarized light, but the plasmon intensity is relatively weak so that the plasmon−plasmon interference is mixed with the plasmon-incident light interference near the center of the spiral. The predominant SPP wave is the short wavelength mode. Again, the simulation demonstrates good agreement with the experiment (simulation movies are available as Supporting Information).

In the final example, we show an $l = 20$ spiral that was created on a 100 μm thick gold film where the long wavelength mode dominates. Figure 9 shows the 2PPE−PEEM images at three different pulse delays when illuminated with RCP light. The first plasmon pulse is seen to spiral inward (Figure 9a) where it creates a 20-point interference ring that rotates about the center (Figure 9b), after which the wave spirals out again (Figure 9c). The numerical model also shows this behavior (Figure 9d−f; refer to the Supporting Information for a simulation movie). In Figure 10 we show the real part of $e^{i20\phi}J_{20}(\alpha' r)$ as a function of position with $\alpha' = 8.03 \times 10^{-3}$ nm^{-1}. This demonstrates the dark central region, associated with the functional form of the Bessel function, and the 20 bright maxima that correspond to the overlap of the first

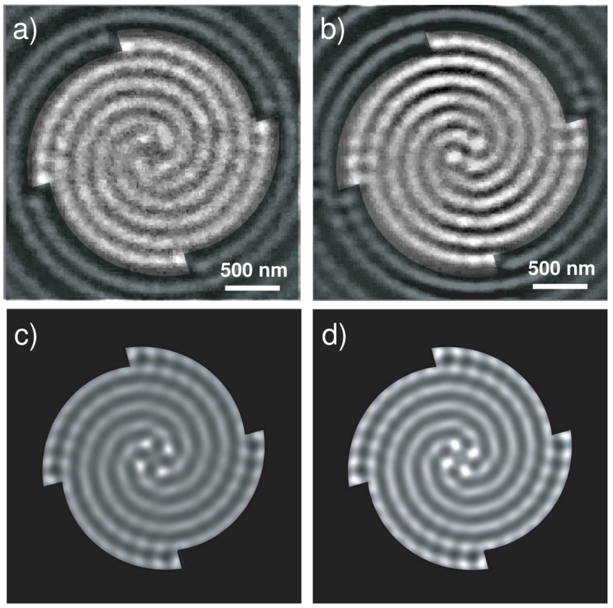

Figure 8. 2PPE−PEEM experiment (a, b) and simulation (c, d) for a spiral with a $4 \times 2\pi = 8\pi$ phase shift anticlockwise around the boundary. (a) Left circular polarization (electric field rotating anticlockwise in the plane); (b) Right circular polarization; (c) simulation LCP; (d) simulation RCP. The experimental images have been masked to highlight the plasmon spiral region; outside this region is the coupling grating and an outward propagating plasmon.

maximum of the Bessel function and the maxima of Re$e^{i20\phi} = \cos(20\phi)$, where ϕ is the angle about the center.

CONCLUSIONS

We have analyzed the excitation and propagation of surface plamon waves excited on metal films by femtosecond pump−probe light pulses including their mutual interference and the subsequent two-photon emission of electrons that are imaged in an electron microscope. We developed an extremely fast, accurate and numerically efficient model of the process showing that most of the observed effects arise from the interference between the electric field of the probe pulses and the vector electric fields of the surface plasmons. The model explains the important features of the PEEM images, such as the SPP waves close to the excitation boundary that remain stationary with pulse delay, and oscillations initiated by the original pump pulse that propagate with a phase determined by the pulse delay. For weak plasmon amplitudes, the model shows that the electric field of the probe must be aligned with the electric field of the surface plasmon, so that no image is expected when the field directions are perpendicular. This is a necessary condition for the electric fields to interfere. Under conditions where there is plasmon focusing, the plasmon fields can be strong enough to initiate electron emission without interaction with the incident light. This is observed by interference effects that change with the helicity of the circularly polarized incident light.

EXPERIMENTAL SECTION

Device Fabrication. The samples were fabricated using single crystal gold platelets. The single crystalline gold platelets were synthesized electrochemically by dissolving a gold wire into a hydrochloric acid based electrolyte. During the reaction, the gold platelets precipitate onto a silicon substrate which has a 2.5 nm thick native oxide layer. The structures in Figures 6, 9,

DOI: 10.1021/acsphotonics.7b00676
ACS Photonics XXXX, XXX, XXX−XXX

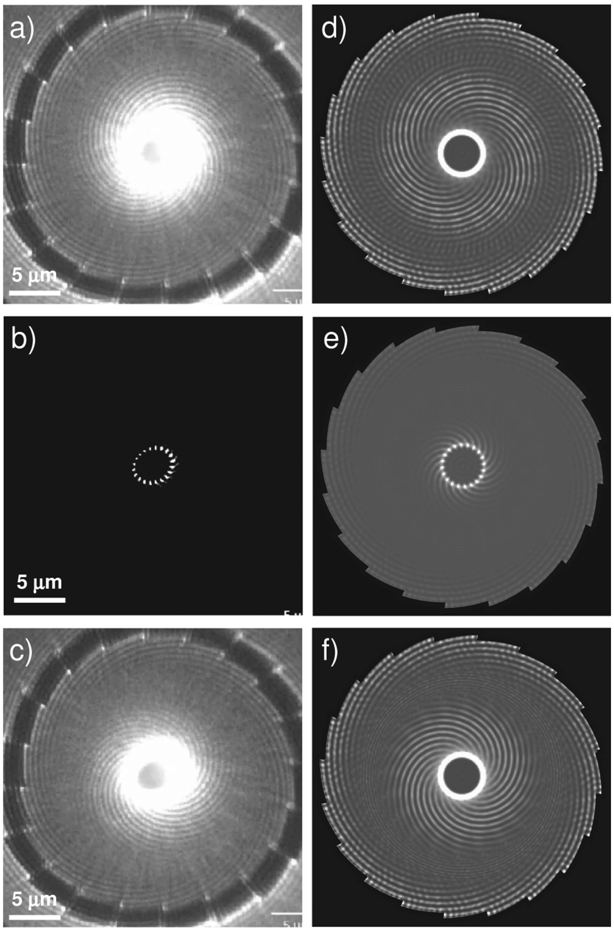

Figure 9. 2PPE−PEEM experiment (a−c) and simulation d-f) for a spiral with a $20 \times 2\pi = 40\pi$ phase shift clockwise around the boundary. The incident light was RCP. (a) 30 fs time delay between the light pulses; (b) 65 fs time delay. The image was rescaled to highlight the central ring pattern; (c) 80 fs time delay; (d−f) simulations corresponding to a−c, respectively.

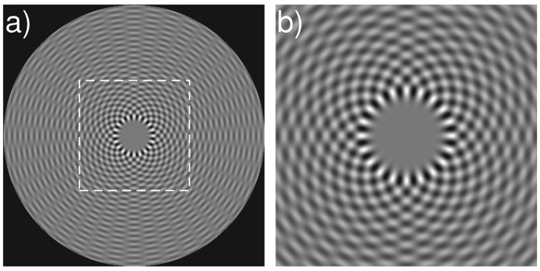

Figure 10. Simulated image of the $l = 20$ spiral of Figure 9 based on the approximate solution $\cos(20\phi)J_{20}(\alpha' r)$, with $\alpha' = 8.03 \times 10^{-3}$ nm^{-1} showing the dark central disk and the 20 bright maxima surrounding it. (a) Full area corresponding to the experiment; (b) enlarged central region, shown by the dashed lines in (a).

and 10 are milled out of a single crystalline gold platelet of 20 nm thickness utilizing a focused gallium ion beam (FIB). FIB milling is performed on the FEI Helios 600 D 534 Machine located at the Institute of Applied Optics, University of Stuttgart.

2PPE−PEEM Measurement. The experiments were performed using the time-resolved photoemission microscope (PEEM) at the University of Duisburg-Essen. In brief, the microscope detects the spatial distribution of photoelectrons liberated via a nonlinear electron emission process induced by a femtosecond laser pulse. To image SPPs at their native wavelength, we use normal incidence of the laser pulses relative to the surface plane.[33] Time-resolved experiments are possible in a pump−probe scheme, where (simplified) a first laser pulse excites a SPP wave, while a second, delayed, laser pulse may liberate a photoelectron. Our optical setup, centered around a Pancharatnam's phase stabilized interferometer, has been described previously[39] and provides us with a relative temporal accuracy of the pump−probe experiment of <50 attoseconds. With such time-resolution, it is possible to image the propagation and interaction of SPPs in slow-motion.[36]

■ ASSOCIATED CONTENT

Supporting Information

The Supporting Information is available free of charge on the ACS Publications website at DOI: 10.1021/acsphotonics.7b00676.

Supplemental pdf: Brief description of the calculation of 2PPE−PEEM simulation movies and calculation times. Figure 4.mp4: Simulation of PEEM data of short-range plasmons excited from a circular boundary. Figure 7lcp.mp4: Simulation of PEEM data of short-range plasmons excited with left circularly polarized light on a spiral boundary with a 2π phase shift. Figure 7rcp.mp4: As above but with right circularly polarized light. Figure 8lcp.mp4: Simulation of PEEM data of short-range plasmons excited with left circularly polarized light on a spiral boundary with a $4 \times 2\pi$ phase shift. Figure 8rcp.mp4: As above but with right circularly polarized light. Figure 9rcp.mp4:Simulation of PEEM data of long-range plasmons excited with right circularly polarized light on a spiral boundary with a $20 \times 2\pi$ phase shift (ZIP).

■ AUTHOR INFORMATION

Corresponding Authors

*E-mail: timd@unimelb.edu.au.

*E-mail: meyerzh@uni-due.de. Phone: +49 711 6856 5111. Fax: +49 711 6856 5097.

*E-mail: giessen@physik.uni-stuttgart.de.

ORCID

Timothy J. Davis: 0000-0002-7299-4900

Notes

The authors declare no competing financial interest.

■ ACKNOWLEDGMENTS

The authors acknowledge funding from the European Research Council Advanced Grant "Complexplas", Deutsche Forschungsgemeinschaft (DFG) Programs SPP1391, SFB616, SFB1242, BMBF, and the Baden-Württemberg Stiftung. A Guest Professorship was funded by the Institute for Quantum Science and Technology (IQST) and the Max Planck Institut für Festkörperforschung.

■ REFERENCES

(1) Economou, E. N. Surface Plasmons in Thin Films. *Phys. Rev.* **1969**, *182*, 539−554.

(2) Barnes, W. L.; Dereux, A.; Ebbesen, T. W. Surface plasmon subwavelength optics. *Nature* **2003**, *424*, 824−830.

(3) Novotny, L.; Hecht, B. *Principles of Nano-Optics*; Cambridge University Press, 2006.

(4) Maier, S. A. *Plasmonics: Fundamentals and Applications*; Springer-Verlag: New York, 2007; Chapter 5.

(5) Davis, T. J. Surface plasmon modes in multi-layer thin-films. *Opt. Commun.* **2009**, *282*, 135−140.

(6) Berini, P. Plasmon-polariton waves guided by thin lossy metal films of finite width: Bound modes of symmetric structures. *Phys. Rev. B: Condens. Matter Mater. Phys.* **2000**, *61*, 10484−10503.

(7) Dionne, J. A.; Sweatlock, L. A.; Atwater, H. A.; Polman, A. Plasmon slot waveguides: Towards chip-scale propagation with subwavelength-scale localization. *Phys. Rev. B: Condens. Matter Mater. Phys.* **2006**, *73*, 035407.

(8) Fu, L.; Schweizer, H.; Weiss, T.; Giessen, H. Optical properties of metallic meanders. *J. Opt. Soc. Am. B* **2009**, *26*, B111.

(9) Woolf, D.; Loncar, M.; Capasso, F. The forces from coupled surface plasmon polaritons in planar waveguides. *Opt. Express* **2009**, *17*, 19996−20011.

(10) Sarid, D. Long-Range Surface-Plasma Waves on Very Thin Metal Films. *Phys. Rev. Lett.* **1981**, *47*, 1927−1930.

(11) Burke, J. J.; Stegeman, G. I.; Tamir, T. Surface-polariton-like waves guided by thin, lossy metal films. *Phys. Rev. B: Condens. Matter Mater. Phys.* **1986**, *33*, 5186−5201.

(12) Prade, B.; Vinet, J. Y.; Mysyrowicz, A. Guided optical waves in planar heterostructures with negative dielectric constant. *Phys. Rev. B: Condens. Matter Mater. Phys.* **1991**, *44*, 13556−13572.

(13) Miyazaki, H. T.; Kurokawa, Y. Squeezing visible light waves into a 3-nm-thick and 3-nm-thick and 55-nm-long plasmon cavity. *Phys. Rev. Lett.* **2006**, *96*, 097401.

(14) Yanai, A.; Levy, U. The role of short and long range surface plasmons for plasmonic focusing applications. *Opt. Express* **2009**, *17*, 14270−14280.

(15) Stockman, M. Nanofocusing of Optical Energy in Tapered Plasmonic Waveguides. *Phys. Rev. Lett.* **2004**, *93*, 137404.

(16) Gramotnev, D. K.; Bozhevolnyi, S. I. Nanofocusing of electromagnetic radiation. *Nat. Photonics* **2013**, *8*, 13−22.

(17) Fang, Z.; Peng, Q.; Song, W.; Hao, F.; Wang, J.; Nordlander, P.; Zhu, X. Plasmonic focusing in symmetry broken nanocorrals. *Nano Lett.* **2011**, *11*, 893−897.

(18) Spektor, G.; David, A.; Gjonaj, B.; Bartal, G.; Orenstein, M. Metafocusing by a Metaspiral Plasmonic Lens. *Nano Lett.* **2015**, *15*, 5739−5743.

(19) David, A.; Gjonaj, B.; Blau, Y.; Dolev, S.; Bartal, G. Nanoscale shaping and focusing of visible light in planar metal-oxide-silicon waveguides. *Optica* **2015**, *2*, 1045−1048.

(20) Gjonaj, B.; David, A.; Blau, Y.; Spektor, G.; Orenstein, M.; Dolev, S.; Bartal, G. Sub-100 nm focusing of short wavelength plasmons in homogeneous 2D space. *Nano Lett.* **2014**, *14*, 5598−5602.

(21) Hachtel, J. A.; Davidson, R. B., II; Chisholm, M. F.; Lawrie, B. J.; Haglund, R. F.; Pantelides, S. T. Unveiling Complex Plasmonic Resonances in Archimedean Nanospirals through Cathodoluminescence in a Scanning Transmission Electron Microscope. *Microsc. Microanal.* **2016**, *22*, 266−267.

(22) Schmidt, O.; Bauer, M.; Wiemann, C.; Porath, R.; Scharte, M.; Andreyev, O.; Schönhense, G.; Aeschlimann, M. Time-resolved two photon photoemission electron microscopy. *Appl. Phys. B: Lasers Opt.* **2002**, *74*, 223−227.

(23) Kubo, A.; Onda, K.; Petek, H.; Sun, Z.; Jung, Y. S.; Kim, H. K. Femtosecond imaging of surface plasmon dynamics. *Nano Lett.* **2005**, *5*, 1123−1127.

(24) Meyer zu Heringdorf, F.; Chelaru, L. I.; Möllenbeck, S.; Thien, D.; Horn-von Hoegen, M. Femtosecond photoemission microscopy. *Surf. Sci.* **2007**, *601*, 4700−4705.

(25) Kubo, A.; Pontius, N.; Petek, H. Femtosecond microscopy of surface plasmon polariton wave packet evolution at the silver/vacuum interface. *Nano Lett.* **2007**, *7*, 470−475.

(26) Meyer zu Heringdorf, F.-J.; Kahl, P.; Makris, A.; Sindermann, S.; Podbiel, D.; Horn-von Hoegen, M. Signatures of plasmoemission in two photon photoemission electron microscopy. *Proc. SPIE* **2015**, *9361*, 93610W.

(27) Podbiel, D.; Kahl, P.; Heringdorf, F.-j. M. Analysis of the contrast in normal-incidenc surface plasmon photoemission microscopy in a pump-probe experiment with adjstable polarization. *Appl. Phys. B: Lasers Opt.* **2016**, *122*, 90.

(28) Spektor, G.; Kilbane, D.; Mahro, A. K.; Frank, B.; Ristok, S.; Gal, L.; Kahl, P.; Podbiel, D.; Mathias, S.; Giessen, H.; Meyer zu Heringdorf, F.-J.; Orenstein, M.; Aeschlimann, M. Revealing the subfemtosecond dynamics of orbital angular momentum in nanoplasmonic vortices. *Science* **2017**, *355*, 1187−1191.

(29) Höfer, U.; Shumay, I. L.; Reuß, C.; Thomann, U.; Wallauer, W.; Fauster, T. Time-Resolved Coherent Photoelectron Spectroscopy of Quantized Electronic States on Metal Surfaces. *Science* **1997**, *277*, 1480−1482.

(30) Petek, H.; Ogawa, S. Femtosecond time-resolved two-photon photoemission studies of electron dynamics in metals. *Prog. Surf. Sci.* **1997**, *56*, 239−310.

(31) Frank, B.; Kahl, P.; Podbiel, D.; Spektor, G.; Orenstein, M.; Fu, L.; Weiss, T.; Michael, H. H.; Davis, T.; Frank-J, M. z. H.; Giessen, H. Short-range surface plasmonics: Localized electron emission dynamics from a 60-nm spot on an atomically flat single-crystalline gold surface. *Sci. Adv.* **2017**, *3*, 1700721.

(32) Dvorak, M.; Schroeder, W.; Andersen, D.; Smirl, A. L.; Wherrett, B. Measurement of the anisotropy of two-photon absorption coefficients in zincblende semiconductors. *IEEE J. Quantum Electron.* **1994**, *30*, 256−268.

(33) Kahl, P.; Wall, S.; Witt, C.; Schneider, C.; Bayer, D.; Fischer, A.; Melchior, P.; Horn-von Hoegen, M.; Aeschlimann, M.; Meyer zu Heringdorf, F. J. Normal-Incidence Photoemission Electron Microscopy (NI-PEEM) for Imaging Surface Plasmon Polaritons. *Plasmonics* **2014**, *9*, 1401−1407.

(34) Morse, P. M.; Feshback, H. *Methods of Theoretical Physics*; McGraw-Hill Book Company Inc.: New York, 1953.

(35) Podbiel, D.; Kahl, P.; Makris, A.; Frank, B.; Sindermann, S.; Davis, T.; Giessen, H.; Horn-von Hoegen, M.; Meyer zu Heringdorf, F. Imaging the Nonlinear Plasmoemission Dynamics of Electrons from Strong Plasmonic Fields. *Nano Letters* **2017** Submitted for publication.

(36) Kahl, P.; Podbiel, D.; Schneider, C.; Makris, A.; Sindermann, S.; Witt, C.; Kilbane, D.; Hoegen, M.-v.; Aeschlimann, M.; zu Heringdorf, F. M. Direct Observation of Surface Plasmon Polariton Propagation and Interference by Time-Resolved Imaging in Normal-Incidence Two Photon Photoemission Microscopy. *Plasmonics* **2017**, na.

(37) Bliokh, K.; Niv, A.; Kleiner, V.; Hasman, E. Geometrodynamics of spinning light. *Nat. Photonics* **2008**, *2*, 748−753.

(38) Bliokh, K.; Rodriguez-Fortuno, F.; Nori, F.; Zayats, A. Spin-orbit interactions of light. *Nat. Photonics* **2015**, *9*, 796−808.

(39) Meyer zu Heringdorf, F.-J.; Podbiel, D.; Raß, N.; Makris, A.; Buckanie, N. M.; Kahl, P. A. Spatio-temporal imaging of surface plasmon polaritons in two photon photoemission microscopy. *Proc. SPIE* **2016**, *992110*, 992110−992118.

DOI: 10.1021/acsphotonics.7b00676
ACS Photonics XXXX, XXX, XXX−XXX